Modelling of heat and mass transfer in a granular medium during high-temperature air drying. Effect of the internal gas pressure

Hammouda Othmani, Lamine Hassini *, Raja Lamloumi, Mohamed Afif El Cafsi

University of Tunis El Manar, Faculté des sciences de Tunis, Laboratoire d'énergétique et des transferts thermique et massique, Tunis, Tunisia

A R T I C L E   I N F O

A B S T R A C T

A comprehensive internal heat and water transfer model including the gas pressure effect has been proposed in order to improve the industrial high-temperature air drying of inserts made of agglomerated sand. In this model, the internal gas phase pressure effect was made perfectly explicit, by considering the liquid and vapour transfer by filtration and the liquid expulsion at the surface. Wet sand enclosed in a tight cylindrical glass bottle dried convectively at a high temperature was chosen as an application case. The model was validated on the basis of the experimental average water content and core temperature curves for drying trials at different operating conditions. The simulations of the spatio-temporal distribution of internal gas pressure were performed and interpreted in terms of product potential damage. Based on a compromise between the drying time and the pressure increase, a simple drying cycle was implemented in order to optimize the drying process.

© 2015 Académie des sciences. Published by Elsevier Masson SAS. All rights reserved.

1. Introduction

The context of this study is the application of high-temperature heating for drying enhancement of agglomerated sand used as container inserts for industrial purposes. The wet agglomerate used as a filling material for containers is composed in general of calibrated sand and of the aqueous solution of a mineral binder. The goal was to predict the spatio-temporal evolution of the moisture content, the temperature and the internal gas pressure within the wet agglomerate sand. The product damage was supposed to be entirely due to the gas phase (vapour and air) overpressure inside the sample [1]. To accelerate the industrial drying of the containers' interiors, it is intended to use intensive drying conditions, like high-temperature convective drying. In this way, the core temperature can quickly reach the water boiling point [2]. In this case, the intense water vaporization induces a strong rise in the pressure of the internal gas phase (vapour and air); such pressure literally pushes the water within and out of the product, which increases very significantly the drying rate [3,4]. However, the internal overpressure that exerts a stress on the material can be a cause of cracking and a compromise must be sought between the drying rate and the pressure raise while defining the operating conditions. The work was carried out in three steps. First, an internal heat and mass transfer model was developed, mainly based on the equations of Constant et al. [5] and Perré and Turner [6]. In this model, the boundary conditions must be adapted in a way that enables liquid water ex-

---

* Corresponding author.
  E-mail address: hassini_lamine@yahoo.fr (L. Hassini).

List of symbols

C_p^{eq}	Equivalent specific heat capacity of the product .... J/kg/K		P_g	Total pressure of the gas phase within the product .... Pa
C_{pl}	Specific heat capacity of liquid water .. J/kg/K		P_v	Water vapour pressure within the product Pa
D_v^{eq}	Equivalent water vapour diffusivity of the product .... m^2/s		R	Ideal gas constant .... J/mol/K
			t	Time .... s
h	Heat transfer coefficient at the product surface .... W/m^2/K		T	Product temperature .... °C, K
			X	Product water content dry basis .... kg/kg
h_m	Mass transfer coefficient at the product surface .... m/s			

Greek symbols

K_g^{eq}	Equivalent gas phase permeability of the product .... m^2		Δh_{des}	Specific differential enthalpy of water desorption .... J/kg
K_l^{eq}	Equivalent liquid phase permeability of the product .... m^2		Δh_{vap}	Specific differential enthalpy of water vaporization .... J/kg
M_a	Air molar mass .... kg/mol		ϕ_0	Dry product total porosity
M_v	Water vapour molar mass .... Pa		λ_{eq}	Equivalent thermal conductivity of the product .... W/m/K
n	Mass flux .... kg/m^2/s		ν_l	Kinematic viscosity of liquid water ...... m^2/s
P_{atm}	Atmospheric pressure .... Pa		ρ_0	Dry product apparent density .... kg/m^3
P_c	Capillary pressure within the product ...... Pa		ρ_l	Liquid water density .... kg/m^3

pulsion at the surface. This adaptation is generally omitted or not explicated in the literature and, to our best knowledge, only Constant et al. [5] considered it and give some precisions about its implementation. Second, the model was validated by comparing the experimental and simulated mean water content in the product and the core temperature curves. The application material was wet sand enclosed in a cylindrical glass bottle. The drying trials were realized in a laboratory hot-air drying tunnel. The equations of our model were solved by means of the COMSOL "Multiphysics" software (v. 3.5), but using the open "PDE coefficient form" mode and not the predefined heat and mass transfer modules. Finally, the model was used to simulate the spatio-temporal evolution of the state variables within the material during the drying process. Based on these simulations, an optimized simple drying schedule was implemented.

2. Methods

2.1. Internal transfer model

The mathematical model proposed in this paper for describing the physical phenomena involved in hygroscopic capillary porous medium subjected to high-air-temperature drying was based on the macroscopic approach of Whitaker [7]. This theory has been successfully adapted and applied to several configurations of granular medium drying, including configuration, which generates intense mass transfer due to an important internal overpressure. The internal heat and mass transfer model was based on the equations of Constant et al. [5] and Perré and Turner [6]. A special emphasis will be applied to the boundary conditions because of the 'water pumping' phenomenon. The formulation of the boundary conditions is one of the original contributions to this study.

2.1.1. Water transfer
The liquid phase flows by filtration due to the gas phase pressure (P_g) gradient and by capillarity due mainly to the liquid water content (X) gradient (the influence of the temperature gradient on the capillary flow is neglected). The liquid flux is thus given by:

$$n_l = -\frac{K_l^{eq}}{\nu_l} \, \text{grad} \, P_g + \frac{K_l^{eq}}{\nu_l} \frac{\partial P_c}{\partial X} \, \text{grad} \, X \tag{1}$$

where K_l is the product liquid permeability, ν_l is the liquid viscosity, P_c is the capillary pressure (as a function of the water content X).

The transfer equation is obtained by inserting the above flux expression in the local mass balance equation and is written as follows:

$$\rho_0 \frac{\partial X}{\partial t} = -\text{div}(n_l + n_v) \tag{2}$$

In equation (2), n_v is the flux of water vapour. The vapour is supposed to move by filtration due to the gas phase pressure gradient, by thermo-diffusion due to the temperature gradient and by ordinary diffusion due to the water content gradient. This flux is hence given by:

$$n_v = k_{41} \operatorname{grad} T + k_{42} \operatorname{grad} X + k_{43} \operatorname{grad} P_g \tag{3}$$

In order to reduce the length of this equation, the numerous physical parameters representing the medium properties were grouped into three global coefficients (k) that are given in Appendix A.

2.1.2. Full equations' system

The model consists finally of five PDEs: the heat transfer equation determining the temperature (T), the liquid water transfer equation determining the liquid water content (X), the dry air transfer equation determining the gas pressure (P_g), and the water vapour transfer equation determining the mass of liquid water vaporized per unit volume (m_{vap}). The full set of equations describing the heat and water transfer within the product writes:

Heat transfer

$$m_{11} \frac{\partial T}{\partial t} + m_{14} \frac{\partial m_{vap}}{\partial t} = \operatorname{div}(k_{11} \operatorname{grad} T) - n_l C_{pl} \operatorname{grad} T \tag{4}$$

Liquid water transfer

$$m_{22} \frac{\partial X}{\partial t} = \operatorname{div}(k_{21} \operatorname{grad} T + k_{22} \operatorname{grad} X + k_{23} \operatorname{grad} P_g) \tag{5}$$

Dry air transfer

$$m_{31} \frac{\partial T}{\partial t} + m_{32} \frac{\partial X}{\partial t} + m_{33} \frac{\partial P_g}{\partial t} = \operatorname{div}(k_{31} \operatorname{grad} T + k_{32} \operatorname{grad} X + k_{33} \operatorname{grad} P_g) \tag{6}$$

Water vapour transfer

$$m_{44} \frac{\partial m_{vap}}{\partial t} = \operatorname{div}(k_{41} \operatorname{grad} T + k_{42} \operatorname{grad} X + k_{43} \operatorname{grad} P_g) \tag{7}$$

As stipulated in the introduction section, the gas pressure gradient appears clearly as one of the transfer driving forces. The term $\partial m_{vap}/\partial t$ in equations (4) and (7) represents the liquid-to-vapour phase change rate term. This term is not the accumulation term for vapour mass. The accumulation of vapour mass in a control volume was neglected. The exact expressions of the m 'capacity' and k 'conductance' coefficients pertaining to the above five transfer equations are given in Appendix A.

2.1.3. Boundary conditions

In order to account for the important phenomenon of liquid water expulsion (called also 'water pumping' in the literature), the water balance equation at the opened product surface was written in the following way:

$$(n_l + n_v)|_{surf} = h_m \frac{P_{atm} M_v}{R T_a} \ln\left(\frac{P_{atm} - P_{va}}{P_{atm} - P_{vsurf}} \right) - \frac{K_l^{eq}}{v_l} \frac{\partial P_g}{\partial n} \bigg|_{surf} \tag{8}$$

where n is the water flux (l for liquid, v for vapour) arriving at the surface, h_m is the convective mass transfer coefficient, K_l is the liquid permeability of the product, v_l is the liquid viscosity, P_v is the vapour pressure ("a" for air, "surf" for surface), T_a is the air temperature. The novelty of this boundary equation lies in the second term on the right side, which represents the liquid water flux arriving at the surface by filtration due to the gas pressure gradient. Including this term means that liquid water arriving at the surface by filtration leaves the product directly as liquid. Consequently, the liquid water arriving by capillary flow in fact evaporates at the surface and leaves the product by convection (diffusion in the boundary layer) as vapour and evidently the water vapour arriving at the surface leaves the product by convection in the same form. This additional term is non-zero if the gas pressure in the product sub surface layer is higher than the atmospheric pressure. Constant et al. [5] have used a similar formulation but they expressed the water expulsion condition with the liquid pressure ($P_l = P_g - P_c$) and not the gas pressure.

Accordingly to the above water transfer boundary condition (eq. (8)), the heat balance equation at the product free boundary was written as:

$$\lambda^{eq} \frac{\partial T}{\partial n} \bigg|_{surf} + \Delta h_{vap} \frac{K_l^{eq}}{v_l} \frac{\partial P_c}{\partial X} \frac{\partial X}{\partial n} \bigg|_{surf} - c_{pl} T_{surf} \frac{K_l^{eq}}{v_l} \frac{\partial P_g}{\partial n} \bigg|_{surf} = h(T_a - T_{surf}) \tag{9}$$

where λ is the thermal conductivity of the product, Δh_{vap} is the enthalpy of water vaporization, c_{pl} is the specific heat of liquid water, h is the convective heat transfer coefficient. This equation separates clearly the latent heat flux due to evaporation from capillary water (second term on the left side) and the advective heat flux due to liquid water expulsion (third term on the left side).

For the sake of completeness, the boundary condition for the gas transfer has to be mentioned. This condition stands simply that the gas pressure at the product surface equals the atmospheric pressure.
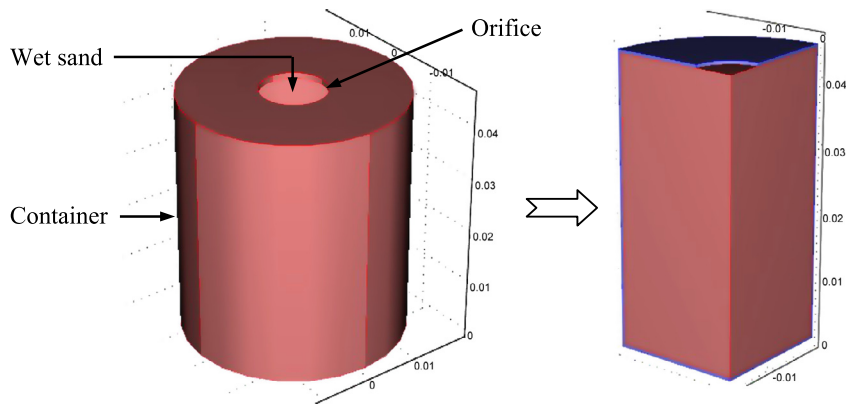
Fig. 1. Computed domain.

Fig. 2. Material preparation for high-temperature air drying.

2.2. Model implementation

Because of the symmetry of the problem, the model was solved on a three-dimensional domain spanning over the quarter of the real domain (see Fig. 1). The governing equations as well as the initial and boundary conditions were numerically implemented in COMSOL Multiphysics finite-elements software (version 3.5a) using the open "PDE coefficient form" mode and not the predefined heat and mass transfer modules.

The computational mesh was defined by means of triangular elements. The direct 'PARDISO out of core' linear system solver was used. Based on the works of Wildenschild and Jensen [8] and Nguyen et al. [9], the sand properties (values or correlations) used in the simulation were detailed in Appendix B.

2.3. Experimental procedures

In order to validate the model, several drying tests were carried out at different operating conditions. Wet sand enclosed in a cylindrical glass bottle with high heat resistance was used. Its height is 3 cm and its diameter base is 4 cm, with a small orifice of diameter 1.5 cm at the center on its top part. This bottle was fabricated especially for these trials. This particular geometry is used in many industrial applications. The surface area for mass exchange with ambient air is extremely small and it is not possible to dry this product in reasonable time without using very intensive conditions like micro-waves or high temperature convection.

The dry sand was enclosed in the container with a funnel and then piled manually. This operation is repeated until the mass of the bottle filled with sand remained constant after two consecutive measurements. Dry piled sand was then impregnated by drip water using a graduated syringe until saturation of the hole and then left for 30 min until the moisture becomes uniform in the product. Fig. 2 shows the different steps of material preparation for high-temperature air drying. The bottle with wet sand was finally placed on a horizontal perforated tray that was suspended to a digital balance, the balance being placed outside the drying chamber. The drying tunnel (designed and realized in the LETTM laboratory, Faculty of Sciences of Tunis) was of vertical type with full control of the drying air parameters (the layout of the dryer is given in a previous paper [10]). The mass and the temperature of the product were continuously measured with constant time interval and recorded by a microcomputer. Each experiment was done at least twice in order to check the reproducibility of the drying curves.
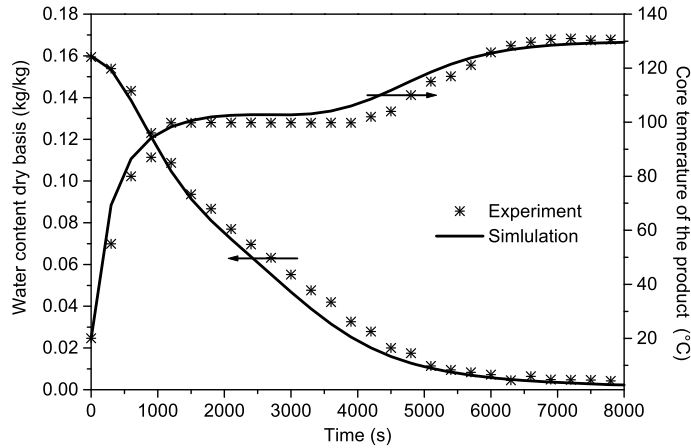
Fig. 3. The average water content and the core temperature of the product versus time ($T_a = 130\,°C$, $u_a = 1$ m/s).

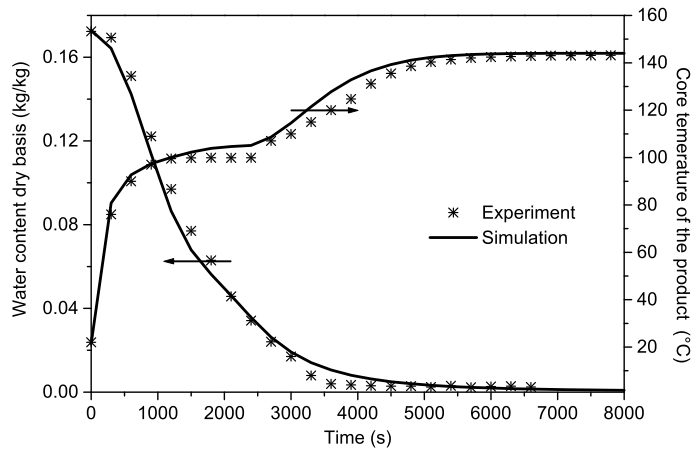**Fig. 4.** The average water content and the core temperature of the product versus time ($T_a = 150\,°C$, $u_a = 1$ m/s).

3. Results and discussion

3.1. Model validation

The method retained to validate our physical model was the comparison of the simulated and experimental drying kinetics (water loss and core product temperature versus time curves) for different drying conditions.

The experimental and simulated temporal evolutions of the mean product water content and core product temperature are shown respectively in Figs. 3 and 4. In general, there was a good agreement between the experimental and simulated results, especially as concerns the core temperature. For all drying conditions, the relative difference between the experimental drying time and the simulated one is less than 10%, which is quite satisfactory. The slight misfit observed could be attributed on the one hand to measurements errors (especially in the mass record due to the support vibration generated by the airflow and in the temperature record due to the imprecision of thermocouple positioning at the core of the sample), and on the other hand to the simplifying hypothesis of the model.

The temperature profile of the sample exhibited a plateau at a value corresponding to the boiling temperature of pure water (around 100 °C) and consecutive internal pressure build-up and water transfer by filtration accompanied by liquid expulsion at the surface.

It must be emphasized that without modifying the formulation of boundary conditions as described in the preceding section, it is not possible to obtain an agreement between experience and simulation for this high-temperature hot air process.

3.2. Simulation of the hydro-thermal state

Numerical modelling allows obtaining the internal profiles of the state variables retained to describe the hydrothermal problem (temperature, water content and internal pressure). The simulation of each one of these variables in three specific
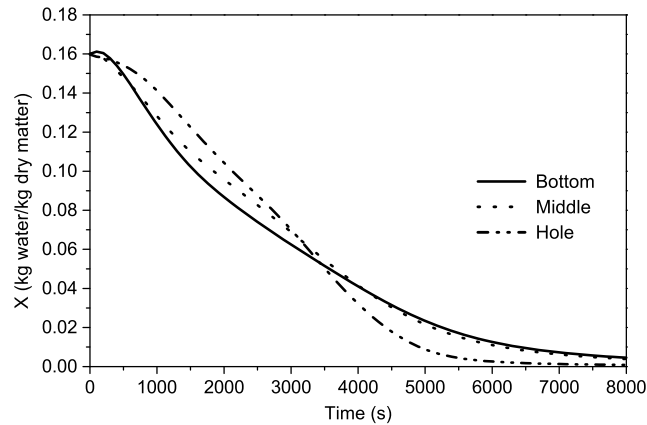
Fig. 5. Simulated spatio-temporal evolution of the water content within the product ($T_a = 120\,°C$, $u_a = 1$ m/s).

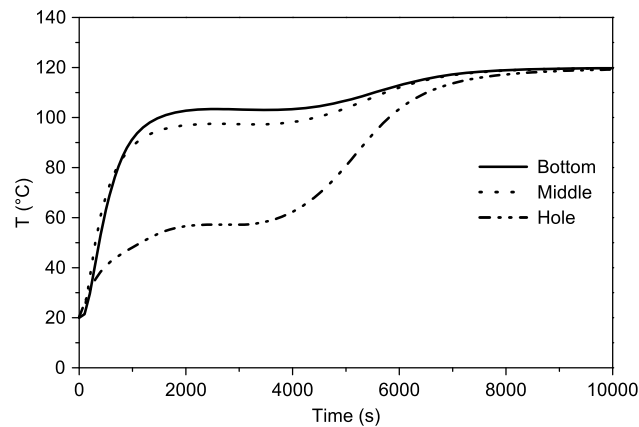**Fig. 6.** Simulated spatio-temporal evolution of the temperature within the product ($T_a = 120\,°C$, $u_a = 1$ m/s).

points of the material (at the bottom, at the middle and at the hole along the axis of revolution) is very interesting in order to understand the physical phenomena that occur during this particular drying process.

The temporal evolution of the average water content at three specific points of the product is depicted in Fig. 5. It can be observed that the moisture gradient in the product is low. This is can be explained by the high moisture diffusivity that redistributes free water in the product during drying. It is also interesting to observe the inversion of the internal water gradient during the course of drying. The water gradient reversal was due to the fact that at the beginning of the drying process water was expulsed directly at the surface in the liquid phase, which was induced by a strong raise of the internal gas phase pressure that pushes water inside and outside the product (a phenomenon that has been observed experimentally). At the end of drying, the product is already partially dry and water transfer at surface occurs only by classical convection.

The temporal evolution of the core temperature at three specific points of the product is shown in Fig. 6. One can observe that the product temperature increased gradually from its initial value to reach a plateau at around 100 °C, corresponding to the transition phenomenon from the liquid phase to the gas phase. At the end of drying, the temperature increases steadily (the energy is converted into sensible heat) to that of the convected air (pseudo-equilibrium with the environment). Besides, the sample temperature profile at the container orifice (dash-dotted curve) exhibited a plateau at a value corresponding probably to the wet-bulb temperature of the hot air (isenthalpic drying phase) because of the existence of liquid water due to the phenomenon of expulsion of liquid at the surface.

3.3. Simulation of the mechanical state via internal gas pressure

The local internal gas pressure curves (bottom, middle and surface) are plotted in Fig. 7. It can be observed that the internal pressure gradient is relatively significant compared to the temperature and water gradients. This shows that water transfer (liquid and vapour) by filtration dominates water transfer by diffusion under a water gradient, for high temperature drying. The pressure rose rapidly at the beginning of drying due to intense water vaporization in the core of the product, and caused the expulsion of the liquid through the permeable sample surface. This was related to the steep slope on the
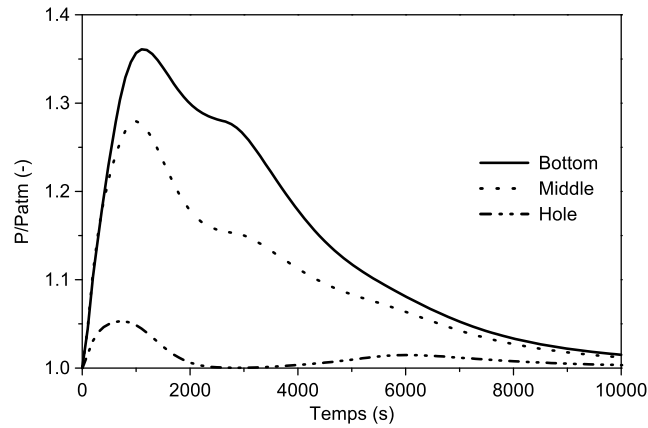
Fig. 7. Simulated spatio-temporal evolution of the pressure within the product ($T_a = 120\,°C$, $u_a = 1$ m/s).
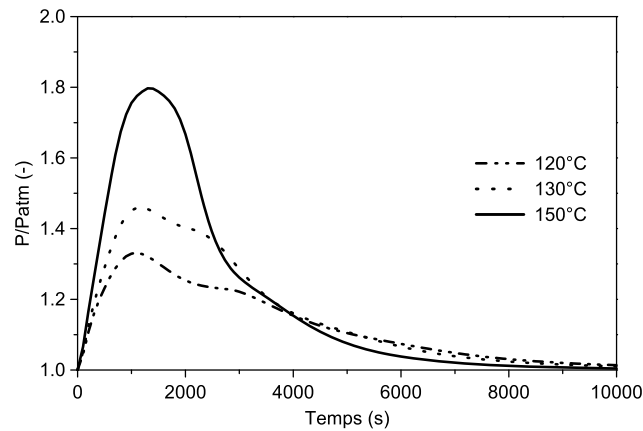

Fig. 8. Simulated spatio-temporal evolution of the pressure within the product at different temperatures ($u_a = 1$ m/s).

loss water curves at the beginning of the process (Figs. 3 and 4). After having attained a maximum, the pressure drops because the free water is scarce and encounters difficulties in reaching the surface of the sample; then gas permeability increases. It should be noted that during high-temperature drying, the internal pressure may be high enough to expulse water directly in the liquid phase at the product surface 'water pumping', providing a kind of mechanical dewatering with non-energy consumption for evaporation.

Assuming that cracking of the material is controlled by the gas phase (air and vapour) overpressure, the product mechanical state can be assessed using internal pressure curves. According to Fig. 7, the maximum pressure level is located in the lower part of the material. The risk of cracking affects only this part. However, the pressure level reaches its maximum at the beginning of drying, the cracks, if they existed, were more likely to appear in the material at the beginning of the process.

The evolution of the internal gas phase pressure at a point situated in the middle of the material with time at different drying temperatures is depicted in Fig. 8. It can be observed that the pressure level depends strongly on the drying temperature. The risk of cracking was thus stronger for a sample dried at a higher temperature.

3.4. Process optimization

According to Figs. 3 and 7, one can observe that intensive drying conditions (internal temperature increase up to beyond the boiling temperature) allowed a faster drying rate, but too much overpressure within the sample. This important internal overpressure exerts a stress on the material and leads sometimes to cracks. This cracking risk associated with such pressure is too high as empirically demonstrated by tests on the tunnel dryer (sample damage). Beside, due to its particular geometry, it is not possible to dry this product in a reasonable time without using very intensive conditions. Thus, a compromise solution must be sought between the drying rate and the pressure increase while defining the optimizing operating conditions. A hot air drying cycle with variable conditions can be a solution for high-temperature drying of particular geometries like that considered here. The scenario proposed consists in general in applying a medium air temperature during the first stage, when the product is almost saturated (to avoid gas pressure rise), a high air temperature afterward, during the second
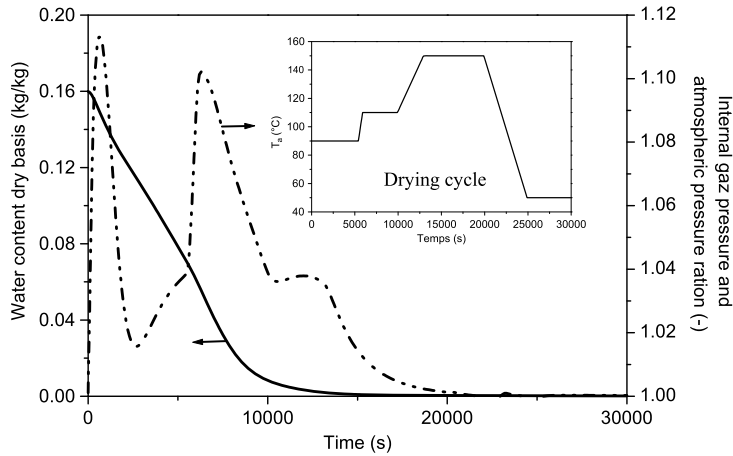
Fig. 9. Optimized drying process.

stage, and finally a low air temperature during the remaining time. Fig. 9 proposed one case of hot air drying cycle with a seven-step process, which can be applied in industry. This cycle allowed for reducing the internal pressure by 36%, but the decrease in the drying time was around 50% with regard to a simple one-stage high-temperature hot air process at 150 °C, which was considered as a reference process. More simulations will have to be done in order to refine and confirm this first result.

4. Conclusion

In order to simulate the high-temperature convection drying of agglomerated sand, a comprehensive internal heat and water transfer model has been proposed. In this model, the internal gas phase pressure effect was made explicit. The transport of liquid and vapour transfer by filtration and liquid expulsion at the surface was considered. The test case was wet sand enclosed in a tight glass container, opened only by a small orifice on its top part and dried convectively. The model was validated on the basis of the experimental mean water content and core temperature curves for drying trials at different conditions. Then, it was used for understanding the physical phenomena that occur in this particular geometry subjected to high-temperature drying related to specific technologies. The product damage was supposed to be entirely due to the gas phase (vapour and air) overpressure. The results demonstrated that the risk of cracking was stronger for a sample dried at a higher temperature. Besides, the cracks were more likely to appear at the upper part of the product. Since a faster drying rate and good quality of dried end-product is beneficial to the agglomerate industry, an optimized drying cycle with variable operating conditions was proposed. This cycle should be refined and validated experimentally before its application in the industry of powder technology.

Appendix A

The coefficients of the model presented in this paper are given below:

$$m_{11} = \rho_0 C_p^{\text{eq}}, \qquad m_{12} = \Delta h_{\text{vap}} + \Delta h_{\text{des}}, \qquad m_{22} = \rho_0$$

$$m_{31} = -\left(\varphi_0 - X\frac{\rho_0}{\rho_{\text{el}}}\right)\frac{M_a}{R}\left[\frac{T\frac{\partial P_v}{\partial T} + P_g - P_v}{T^2}\right]$$

$$m_{32} = -\frac{M_a}{RT}\left[\frac{\partial P_v}{\partial X}\left(\varphi_0 - X\frac{\rho_0}{\rho_{\text{el}}}\right) + \frac{\rho_0}{\rho_{\text{el}}}(P_g - P_v)\right]$$

$$m_{33} = \left(\varphi_0 - X\frac{\rho_0}{\rho_{\text{el}}}\right)\frac{M_a}{RT}$$

$$m_{44} = 1, \qquad m_{55} = \rho_0, \qquad k_{11} = \lambda^{\text{eq}}$$

$$k_{21} = \frac{M_v P_v}{RT}\left(1 - \frac{P_v(M_v - M_a)}{M_v P_v + M_a(P_g - P_v)}\right)\frac{\partial P_v}{\partial T}$$

$$k_{22} = \frac{M_v P_v}{RT}\left(1 - \frac{P_v(M_v - M_a)}{M_v P_v + M_a(P_g - P_v)}\right)\frac{\partial P_v}{\partial X} - \frac{K_l^{\text{eq}}}{\nu_l}\frac{\partial P_c}{\partial X}$$

$$k_{23} = \frac{M_v P_v}{M_v P_v + M_a(P_g - P_v)}\frac{K_g^{eq}}{v_g} - \frac{M_v D_v^{eq}}{RT}\frac{P_v M_a}{M_v P_v + M_a(P_g - P_v)} + \frac{K_l^{eq}}{v_l}$$

$$k_{31} = -\frac{M_v D_v^{eq}}{RT}\left(1 - \frac{P_v(M_v - M_a)}{M_v P_v + M_a(P_g - P_v)}\right)\frac{\partial P_v}{\partial T}$$

$$k_{32} = -\frac{M_v D_v^{eq}}{RT}\left(1 - \frac{P_v(M_v - M_a)}{M_v P_v + M_a(P_g - P_v)}\right)\frac{\partial P_v}{\partial X}$$

$$k_{33} = \frac{M_a(P_g - P_v)}{M_v P_v + M_a(P_g - P_v)}\frac{K_g^{eq}}{v_g} + \frac{M_v D_v^{eq}}{RT}\frac{P_v M_a}{M_v P_v + M_a(P_g - P_v)}$$

$$k_{41} = -\frac{M_v D_v^{eq}}{RT}\left(1 - \frac{P_v(M_v - M_a)}{M_v P_v + M_a(P_g - P_v)}\right)\frac{\partial P_v}{\partial T}$$

$$k_{42} = -\frac{M_v D_v^{eq}}{RT}\left(1 - \frac{P_v(M_v - M_a)}{M_v P_v + M_a(P_g - P_v)}\right)\frac{\partial P_v}{\partial X}$$

$$k_{43} = -\frac{M_v P_v}{M_v P_v + M_a(P_g - P_v)}\frac{K_g^{eq}}{v_g} + \frac{M_v D_v^{eq}}{RT}\frac{P_v M_a}{M_v P_v + M_a(P_g - P_v)}$$

The parameters P_c, P_v, D_v, K_l, K_g, λ, v are product specific functions of state variables X and T.

Appendix B

Semi-empirical equations for product properties

Material property	Value or correlation	
Total porosity of the dry product	$\varphi_0 = 0.35$	
Tortuosity of the dry product	$\tau_0 = 2$	
Specific permeability of the product	$K_0 = 10^{-13}$ (m^2)	
Apparent density of the dry product	$\rho_0 = 1757$ (kg/m^3)	
Apparent density of the liquid phase	$\rho_l = 1000$ (kg/m^3)	
Equivalent specific heat capacity of the product	$C_p^{eq} = 900 + 4180X$ (J/kg/K)	
Relative permeability of the liquid phase	$K_{rl} = S^{\gamma}(1 - (S^{1/m})^m)^2$	$n = 5.2$, $m = 1 - 1/n$
Relative permeability of the gas phase	$K_{rg} = (1 - S)^{\gamma}(1 - S^{1/m})^{2m}$	$g = 9.81$ m/s^2, $\alpha = 0.029$
Capillary pressure in the product	$P_c = (\rho_l g/\alpha)(S^{-1/m} - 1)^{1/n}$ (Pa)	$\gamma = 0.25$, $S = X/X_{sat}$
Equivalent conductivity of the product	$\lambda^{eq} = 0.9$ (W/m/K)	
Equivalent water vapour diffusivity of the product	$D_v^{eq} = (\phi_0/\tau_0)K_{rl}D_{va}$ (m^2/s)	
Specific differential enthalpy of water vaporization	$\Delta h_{vap} = 4187(597.3 - 0.592(T - 273))$ (J/kg)	
Specific differential enthalpy of water desorption	$\Delta h_{des} = 30{,}107\exp(-482.1859X)$ (J/kg)	
Partial pressure of water vapour in the product	$P_v = a_w P_{vsat}$ (Pa), $a_w = 1$ (non-hygroscopic material)	
Saturation moisture content	$X_{sat} = \varphi_0(\rho_l/\rho_s)$ (kg/kg)	

References

[1] S.J. Kowalski, B. Mielniczuk, Analysis of effectiveness and stress development during convective and microwave drying, Dry. Technol. 26 (1) (2007) 64–77.
[2] P. Salagnac, P. Glouannec, D. Lecharpentier, Numerical modeling of heat and mass transfer in porous medium during combined hot air, infrared and microwaves drying, Int. J. Heat Mass Transf. 47 (2004) 4479–4489.
[3] P. Perré, C. Moyne, Processes related to drying: part II: use of the same model to solve transfers in saturated and unsaturated porous media, Dry. Technol. 9 (5) (1991) 1153–1179.
[4] I.W. Turner, C. Jolly, Combined microwave and convective drying of a porous material, Dry. Technol. 9 (5) (1991) 1209–1269.
[5] T. Constant, C. Moyne, P. Perré, Drying with internal heat generation: theoretical aspects and application to microwave heating, AIChE J. 42 (2) (1996) 359–368.
[6] P. Perré, W. Turner, Microwave drying of softwood in an oversized waveguide: theory and experiment, AIChE J. 43 (10) (1997) 2579–2586.
[7] S. Whitaker, Simultaneous heat, mass, and momentum transfer in porous media: a theory of drying, Adv. Heat Transf. 13 (1977) 119–203.
[8] D. Wildenschild, K.H. Jensen, Laboratory investigations of effective flow behavior in unsaturated heterogeneous sands, Water Resour. Res. 35 (1) (1999) 17–27.
[9] T.Q. Nguyen, J. Petkovic, P. Dangla, V. Baroghel-Bouny, Modelling of coupled ion and moisture transport in porous building materials, Constr. Build. Mater. 22 (2008) 2185–2195.
[10] L. Hassini, S. Azzouz, R. Peczalski, A. Belghith, Estimation of potato moisture diffusivity from convective drying kinetics with correction for shrinkage, J. Food Eng. 79 (2007) 47–56.